Small-molecule inhibition of MuRF1 protects against disuse-induced diaphragmatic dysfunction: Underlying molecular mechanisms

Fernando Ribeiro[1], Paulo R. Jannig[2], Siegfried Labeit[3,4], Anselmo S. Moriscot[1*]

[1]Department of Anatomy, Institute of Biomedical Sciences, University of São Paulo, 05508-000 São Paulo, Brazil

[2]Department of Physiology and Pharmacology, Biomedicum, Karolinska Institutet, 171 77 Stockholm, Sweden

[3]Department for Integrative Pathophysiology, DZHK Partner Site Mannheim-Heidelberg, Medical Faculty Mannheim, University of Heidelberg, 68169 Mannheim, Germany

[4]Myomedix GmbH, Neckargemünd, Germany

[*]Correspondent author (e-mail: moriscot@usp.br)

Abstract

Background: Disuse-induced diaphragmatic dysfunction (DIDD) is characterized by the rapid and progressive loss of diaphragm contractile function and mass in response to inactivity. DIDD compromises respiratory function and enhances morbidity and mortality risks in patients undergoing prolonged mechanical ventilation or phrenic nerve injury. Muscle RING-finger protein-1 (MuRF1) expression is rapidly upregulated under diaphragm mechanical unloading, and is hypothesized to play a role in DIDD pathophysiology. We previously reported that small-molecule inhibition of MuRF1 protects against early DIDD in rats. Herein, we investigated the mechanisms underlying MuRF1 inhibition-mediated protection against DIDD in rats.

Methods: Male Wistar rats were subjected to unilateral diaphragm denervation (UDD) for 12 hours to induce DIDD. Immediately after UDD, animals received a placebo (vehicle) or MuRF1 inhibitor (MyoMed-205, 50 mg/kg bw) treatment and were compared with Sham-operated controls. Diaphragm was used for histological, morphometric, transcriptomic (RNA-seq), and protein content (Western Blot) analysis.

Results: UDD induced diaphragm slow- and fast-twitch muscle fiber atrophy (~18%, $p < 0.05$) after 12 hours, which was prevented by MuRF1 inhibition. Mechanistically, UDD perturbed mechanisms involved with myofiber ultrastructure and contractility, mitochondrial function, proteolysis, and tissue remodeling in the diaphragm. Notably, MuRF1 inhibition enhanced mechanisms required for sarcomere integrity, calcium handling, antioxidant defense, chaperone-mediated unfolded protein response, and muscle growth. Moreover, MuRF1 inhibition downregulated intramuscular lipid accumulation and fibrosis responses triggered by prolonged disuse.

Conclusion: Small-molecule inhibition of MuRF1 protects against early DIDD in rats undergoing 12 hours of UDD. Mechanistically, this involved augmented control of

muscle structure and function, chaperone-mediated unfolded protein, and muscle growth factors, while intramuscular fat accumulation and fibrosis responses associated with DIDD were attenuated.

Keywords: Skeletal muscle; unilateral diaphragm denervation; mechanical ventilation; mechanical unloading; muscle atrophy; ubiquitin-proteasome system; TRIM63.

Introduction

Breathing is an essential biological process for life maintenance. This process is regulated by a complex neuromuscular network that generates differential intrathoracic pressures contributing to ventilation and gas exchange. The diaphragm works as the main inspiratory pump, besides also contributing to other important physiological functions (e.g., visceral organization, coughing, and venous hemodynamics). Due to its key role, the diaphragm undergoes a particular evolutionary development, including unique adaptations to its high functional activity throughout life. This in turn leads to a singular response to mechanical unloading (i.e., disuse), in some aspects differing from other skeletal muscles [1]. Disuse-induced diaphragmatic dysfunction (DIDD) can be observed in clinical conditions such as congenital or acquired phrenic nerve injury (e.g., due to thoracic surgery or trauma), as well as in mechanically ventilated critically ill patients. DIDD is characterized by the rapid and progressive loss of diaphragm contractile function and mass, contributing to impaired respiratory capacity, exercise intolerance, poor quality of life, and higher mortality risk [2]. Experimentally, unilateral diaphragm denervation (UDD) has been used to mimic DIDD common features observed in patients subjected to diaphragm paralysis and prolonged stay in the intensive care unit (ICU) for critical illness treatment [3].

The cellular and molecular mechanisms underlying the DIDD's pathophysiology are multifactorial and complex. Mechanical silencing secondary to phrenic nerve injury or mechanical ventilation can rapidly trigger muscle's mechanosensory elements associated with downstream pathways controlling muscle strength and mass [4]. Post-translational modifications of sarcomeric proteins are also known to contribute to the

early diaphragm contractile dysfunction, even preceding significant atrophy [5]. Moreover, mechanical unloading can also disturb diaphragm calcium (Ca^{2+}) handling and sensitivity, mitochondrial dysfunction, oxidative stress, endoplasmic reticulum (ER) stress, and altered zinc ion homeostasis [6–8]. Consequently, increased protein damage and breakdown contribute to a negative protein net balance as a result of disuse-induced inhibition of protein synthesis [9], and enhanced protein degradation via ubiquitin-proteasome system, autophagy, and other proteolytic systems [10,11]. These modifications can ultimately induce apoptosis and diaphragm muscle remodeling, including intramuscular lipid accumulation and fibrosis [12].

Since its discovery during the early 2000s, Muscle RING-finger protein 1 (MuRF1) has been recognized as an important regulator of skeletal muscle mass and function [13,14]. This muscle-specific E3-ligase targets functionally distinct protein clusters involved with the control of muscle contraction, Ca2+ handling, energy metabolism, immune response, and protein breakdown [15–17]. Increased MuRF1 expression and/or activity have been observed in several stress states with underlying muscle wasting and weakness induced by immobilization, denervation, corticosteroids, heart failure, cancer cachexia, or aging. On the other hand, deletion of MuRF1 (knockout models) can significantly improve muscle mass and function (for review, see [18]). In this context, MuRF1 deletion/inhibition has been reported to protect early disuse-induced diaphragmatic dysfunction in mechanically ventilated rodents [10,19]. These findings may indicate that MuRF1 plays a key role in DIDD pathophysiology and represents an attractive therapeutic target.

Over the past decade, the development of small molecules targeting MuRF1 marked a significant advance for exploring the therapeutic potential of MuRF1 inhibition for counteracting muscle wasting and weakness in disease conditions. Previous works suggest that small-molecule inhibition of MuRF1 attenuates muscle wasting and weakness in distinct experimental models for heart failure [20–22], cancer cachexia [23], and muscle myopathies, such as those induced by corticosteroids [20] or type 2 diabetes [24]. Recently, our group reported that small-molecule inhibition of MuRF1 protects against early disuse-induced diaphragm contractile dysfunction and atrophy in the UDD experimental model [25]. Collectively, these findings suggest that small-molecule targeting MuRF1 activity may represent a promising therapeutic strategy to counteract muscle wasting and weakness induced by stress states, such as DIDD.

This study aimed to investigate the cellular and molecular mechanisms underlying MuRF1 inhibition-mediated protection against early DIDD in rats subjected to UDD. We hypothesized that 1) MuRF1 activity plays a key role in DIDD pathophysiology, and 2) MuRF1 inhibition might result in a differential regulation of pathways involved with the control and preservation of muscle and contractile function during the disuse-induced stress state. We found that MuRF1 inhibition stimulated adaptive responses to oxidative stress, to misfolded proteins by activating chaperones, and activated protein synthesis under UDD. Finally, MuRF1 inhibition downregulates pathways associated with intramuscular fat accumulation and ECM collagen deposition. Taken together, MuRF1 inhibition markedly protected against early DIDD following UDD in rats.

Material and Methods

Animals

Wistar rats (Male, 2-3 months old) were used in this study. The animals were kept in standard cages under controlled environmental conditions (24 ± 1°C, 12 h/12 h light-dark cycle) with access to standard food and water *ad libitum*. This study was approved and followed the institutional guidelines for animal care and use for research (CEUA ICB USP #8728030320 and #5143091020).

Experimental design

Twenty-four rats were randomly allocated into three experimental groups (*n* = 8): Sham 12h (Sham); UDD 12 hours + vehicle (DNV + VEH); and UDD 12 hours + MyoMed-205 (DNV + 205). After 12 hours, the animals were euthanized under anesthesia, and the denervated right diaphragm muscle (costal portion) was harvested, quickly snap-frozen in 2-methylbutane chilled in liquid nitrogen, and stored at -80°C until further analysis. Diaphragm samples used in this study originate from our previous work [25] (for further details, see supplementary information).

MuRF1 inhibitor formulation and delivery

A detailed description of MuRF1 inhibitor (MyoMed-205, Myomedix GmbH, Germany) formulation for the *in vivo* study is provided in the supplementary information. Briefly, the compound was freshly dissolved in an 8 mL vehicle solution (DMSO-PEG400-Saline 0.9%). The delivery of either vehicle (VEH) or MyoMed-205 (205) treatments was managed in four split doses (2 mL/dose) administered every 3 h interval over the 12-hour experimental period via the caudal vein. Treatments started immediately

following the confirmation of unilateral diaphragm paralysis (for further details, see supplementary information).

Unilateral diaphragm denervation (UDD)

Animals were initially sedated and anesthetized, and after reaching the surgical plane, the right phrenic nerve was exposed and transected at the rat's lower neck region. The absence of right diaphragm dome contractile activity was used to confirm the denervation's efficacy. Then, the surgical wound was sutured and managed with antiseptic (for further details, see supplementary information).

Diaphragm muscle fiber typing and size analysis

Cryosections (8 μm thick) from the right costal diaphragm muscle were prepared using a cryostat at −20°C (Leica CM1850, Germany). Muscle fiber typing (MyHC I, IIA, IIB/X) was performed via immunofluorescence assay (see antibodies in Table S1). Photomicrographs were acquired using Axio Scope A1 microscope (Zeiss, Germany). Diaphragm fibers' type distribution and cross-sectional area (CSA) were assessed with ImageJ (Fiji, NIH, USA). Representative muscle fiber type distribution and CSA values were determined as the average from 300 fiber measurements per sample (for further details, see supplementary information).

Oil Red O (ORO) Staining

Diaphragm muscle cryosections were stained with ORO to assess the intramuscular lipid content. Photomicrographs were acquired using Axio Scope A1 microscope (Zeiss, Germany). Representative number of positive ORO (ORO+) muscle cells and

intracellular lipid content were determined based on measurements of 300 fibers per sample (for further details, see supplementary information).

Transcriptomic profiling (RNA-seq)

Total RNA was extracted from the diaphragm using TRIzol (Life Technologies, Carlsbad, CA). RNA integrity was analyzed using Bioanalyzer 2100 (Agilent, Santa Clara, CA, USA) (Table S2). Four samples of each experimental group with the highest purity and integrity levels were selected for global gene expression analysis (Figure S1). Approximately ~1 ug of sample total RNA was used for cDNA library preparation performed according to the Illumina mRNA stranded poly-A tail enrichment Kit manufacturer's instructions (Illumina, San Diego, CA). RNA sequencing was carried out using the Illumina NextSeq 2000 (NextSeq 2x100pb, 20 million paired-end reads depth). These procedures were performed by NGS Soluções Genômicas (Piracicaba, Brazil).

For bioinformatic analysis, quality control of raw reads was performed using the FastQC toolkit (Babraham Bioinformatics). The reads were then aligned to the mRatBN7.2 rat genome using STAR. Feature count was performed using featureCounts, and differential expression analyses were generated in R using the DESeq2 package with adaptive log-fold change shrinkage estimator from the ashr package Pathway analysis was carried out by Gene Set Enrichment Analysis (GSEA) using a pre-ranked list of genes by log2Fold-Change and Molecular Signatures Database, and hallmark pathways gene sets for pathway analysis (for further details, see supplementary information).

Western Blotting

Diaphragm samples were powdered in a liquid nitrogen-chilled mortar and homogenized in RIPA buffer containing protease and phosphatase inhibitors (ThermoFisher #78445). Homogenates were centrifuged and the collected and stored at −80°C until further analysis. Protein concentration was determined by the Bradford method with bovine serum albumin (BSA) as the standard. Protein was loaded onto polyacrylamide gel (SDS-PAGE), separated via electrophoresis (100V), and transferred to polyvinylidene difluoride (PVDF) membrane (Thermo Fisher Scientific, #88518, Rockford, IL, USA) using wet-transfer system (100 V, 350 mA, for 120 min). Ponceau red staining was used to assess protein transfer efficacy. Membranes were incubated with primary and secondary antibodies (Table S1). Membranes were incubated with ECL substrate (Immobilon Forte, Millipore #WBLUF0500) for 5 minutes before signal detection using C-digit blot scanner (Li-Cor, USA) for chemiluminescent detection, or with BCIP/NBT substrate (Sigma #B1911) for colorimetric detection. Alpha-tubulin was used as a loading control for data normalization, and densitometry analysis was performed using ImageStudio software (for further details, see supplementary information).

Statistical Analysis

Data analysis was performed Excel, Prism and R. The Shapiro-Wilk test was used to assess data normality. One-way ANOVA followed by Tukey's post-hoc test, or the Kruskal-Wallis followed by Dunn's test, were used for multiple comparisons between groups, respectively for parametric and non-parametric data. Data are presented as mean ± standard deviation and statistical significance was accepted as $p < 0.05$.

Results

Transcriptomic profiling reveals mechanisms underlying MuRF1 inhibition mediated protection against disuse-induced diaphragmatic dysfunction

To investigate how mechanical unloading (i.e., disuse) impairs diaphragm muscle structure and contractile function, and to determine the effects MuRF1 inhibition, we performed a global gene expression analysis of the diaphragm muscle of rats subjected to UDD for 12 h. Animals were treated either with vehicle (DNV_VEH) or MuRF1 inhibitor (DNV_205), and results were compared with Sham-operated controls (Figure 1A).

Principal component analysis (PCA) demonstrated significant transcriptomic alterations in DNV_VEH compared with Sham. On the other hand, MuRF1 inhibition caused no evident changes in the clustering pattern compared with DNV_VEH (Figure 1B). DESeq2 analysis was performed in order to identify differentially expressed genes (DEGs) for each condition (Padj < 0.05). We detected 1563 DEGs in DNV_VEH (873 upregulated, 690 downregulated) and 3487 DEGs in DNV_205 (1935 upregulated, 1552 downregulated), compared with Sham. We found 69 DEGs (7 upregulated, 62 downregulated) were particularly responsive to MuRF1 inhibition compared with DNV_VEH (Figure 1B). Hierarchical clustering analysis revealed five gene clusters regulated by disuse and MuRF1 inhibition (Figure 1C).

Gene Set Enrichment Analysis (GSEA) was subsequently employed to identify biological pathways modulated by disuse and MuRF1 inhibition, including hallmark pathways (Figure 1D), molecular functions (Figure 1E), and cellular compartments

(Figure 1F). Disuse significantly altered the expression of genes associated with muscle contraction, mitochondrial structure/function, inflammatory responses, proteolysis, apoptosis, and muscle tissue remodeling, compared with Sham. Interestingly, MuRF1 inhibition upregulated pathways involved with antioxidant response, chaperone-mediated unfolded protein response, ribosome biogenesis, protein synthesis, and cell growth. Conversely, MuRF1 inhibition downregulates genes associated with adipogenesis and extracellular matrix collagen deposition compared with DNV_VEH and Sham groups (Figure 1D-F).

Effects of MuRF1 inhibition upon mechanisms that control skeletal muscle structure and contractile function

We previously reported that 12 hours of diaphragm disuse induced by UDD promotes muscle contractile dysfunction and atrophy [25]. Herein, our histomorphometric analysis confirmed a significant decrease in diaphragm fiber size across all types (I, IIA, IIB/X) following 12 h of disuse compared with Sham (~18%, $p < 0.05$, $n = 8$), while fiber type distribution remained unchanged (Figure 2A-B). MuRF1 inhibition significantly protected against disuse-induced diaphragm fiber atrophy ($p < 0.05$, $n = 8$) without altering fiber type distribution (Figure 2B).

To gain mechanistic insights into the protective effects of MuRF1 inhibition, we examined the expression levels of genes and proteins involved in the control of muscle structure and contraction. Significant changes in genes regulating synaptic vesicle membrane and muscle fiber structure/function were observed following 12 h of disuse (Figure 2C). Noteworthy, MuRF1 inhibition selectively enhanced the expression of genes involved with sarcomere organization and integrity, Z-disk structure,

mechanotransduction, and intercellular communication (e.g., Tcap, Actn1, Pdlim3, Cryab, Ankrd1, Zyx, Sdc4, Sorbs1, Tpm4, Bag3 and Gja1) (Figure 2C-D).

Furthermore, disuse significantly disrupted calcium handling pathways as indicated by downregulation of key calcium handling genes (e.g., RyR1, SERCA1, and SERCA2) (Figure 2E) and increased phospholamban protein levels compared with Sham (Figure 2F). MuRF1 inhibition enhanced S100A1 expression, a calcium-binding protein that positively regulates the activity of calcium channels, concomitantly with suppression of disuse-induced phospholamban expression (Figure 2E-F).

Disuse promotes mitochondrial dysfunction and oxidative stress, while MuRF1 inhibition enhances the expression of antioxidant factors

Mitochondrial structure and function are essential for the maintenance of skeletal muscle function and homeostasis. Therefore, we assessed mitochondrial alterations following 12 h of disuse and MuRF1 inhibition in the diaphragm. Disuse significantly impaired mitochondrial structure and function at the transcriptional level after 12 hours. Key mitochondrial biogenesis regulators (e.g., Ppargc1a) and dynamics mediators (e.g., Opa1, Mfn1, Mfn2) were markedly downregulated (Figure 3A). Genes encoding mitochondrial structural complexes (Figure 3B-C), as well as those regulating energy metabolism via oxidative phosphorylation and fatty acid oxidation (Figure 3D) were also markedly downregulated, further suggesting the rapid development of mitochondrial dysfunction. Moreover, we observed increased activation of reactive oxygen species (ROS) pathway (Figure 3E). Interestingly, MuRF1 inhibition upregulated a subset of genes involved with the redox balance and antioxidant response (e.g., Nrf1, Nfe2l2, Sirt1, Sod2, Prdx1, Prdx6, and Gclc) (Figure 3E).

MuRF1 inhibition enhances activation of pathways regulating ribosome biogenesis, protein synthesis and cell growth under disuse stress

Disuse negatively affects diaphragm muscle mass by inhibiting protein synthesis, leading to a negative protein net balance. We evaluated the impacts of disuse and the MuRF1 inhibition upon pathways involved with cell growth, proliferation, and survival. Noteworthy, Myc target genes (Figure 4A), the KRAS (Figure S3), and mTORC1 signaling pathways were found upregulated after 12 hours of disuse (Figure 4B). Strikingly, MuRF1 inhibition enhanced RNA processing and transcription (Figure S2), further amplifying these effects by increasing the expression of genes associated with the PI3K-Akt-mTOR pathway (Figure 4B), ribosome biogenesis, translation initiation (Figure 4C), and androgen response (Figure S3). Consistent with gene expression changes, MuRF1 inhibition increased PI3K-Akt-mTOR pathway activation at the protein level (Figure 4D).

Disuse upregulates proteolytic signaling pathways while MuRF1 inhibition improves chaperone-mediated unfolded protein response

Disuse also activates proteolytic pathways contributing to diaphragm muscle wasting. Thus, we evaluated the effect of disuse and the MuRF1 inhibition upon pathways associated with muscle protein breakdown and programmed cell death. Disuse significantly upregulated distinct proteolytic and stress response pathways, including immune and inflammatory responses (Figure S4), the IL6-JAK-STAT3 pathway (Figure 5A), unfolded protein response (Figure 5B), ubiquitin-proteasome pathway (Figure 5C-D), p53 pathway (Figure 5E), and apoptosis (Figure 5F). Remarkably, MuRF1 inhibition enhanced the expression of genes mediating chaperone-mediated

unfolded protein response (Figure 5B). Unexpectedly, MuRF1 inhibition resulted in a relatively higher expression of E3-ligases linked to muscle wasting, including Fbxo32 (i.e., Atrogin-1, log2fold = 0.96 vs 0.20, values relative to Sham; padj = 0.59) and TRIM63 (i.e., MuRF1, log2fold = 2.27 vs 1.44, values relative to Sham; padj = 0.59) compared with DNV_VEH, despite not reaching statistical significance (Figure 5C). In line with this, protein levels of these E3-ligases and K48-ubiquitinated proteins were not significantly changed, except for MuRF2, a close relative of MuRF1, which was upregulated by disuse but blocked under MuRF1 inhibition (Figure 5D).

MuRF1 inhibition blocks disuse-induced expression of genes associated with intramuscular lipid accumulation and ECM-collagen deposition

Prolonged disuse can lead to sustained cell stress and damage, triggering apoptosis and tissue remodeling responses such as intramuscular fat deposition and fibrosis. Therefore, we evaluated how disuse and MuRF1 inhibition affect these responses in the diaphragm.

After 12 h of disuse, we observed a significant upregulation in adipogenic-related gene expression compared with Sham (Figure 6A), although no changes were detected in adipogenic or lipid droplet-related proteins within this period (Figure 6B). Oil Red O (ORO) staining revealed significantly increased ORO-positive (ORO+) cells and intracellular lipid content across distinct fiber phenotypes (i.e., predominantly oxidative fibers <2500 μm², and predominantly glycolytic fibers >2500 μm²). Interestingly, MuRF1 inhibition suppressed adipogenesis (Figure 6A), mitigating intramuscular lipid accumulation following disuse (Figure 6C).

Moreover, disuse also upregulated the expression of genes associated with the TGF-β signaling (Figure S5), collagen trimmer (Figure 7A), basement membrane (Figure 7B), and extracellular-matrix collagen deposition (Figure 7C), compared with Sham. On the other hand, MuRF1 inhibition suppressed these disuse-induced pro-fibrotic responses (Figure 7A-C).

Discussion

Mechanical unloading rapidly induces diaphragm muscle contractile dysfunction and atrophy, contributing to impaired respiratory function, morbidity, and mortality. This clinical condition is particularly found in patients undergoing phrenic nerve injury or prolonged mechanical ventilation during ICU treatment. Therefore, understanding the mechanisms underlying DIDD pathophysiology and how to prevent them by potential novel therapeutic targets is an important, and yet unmet, clinical need. We recently reported that small-molecule inhibition of MuRF1 protects against early DIDD in rats subjected to UDD [25]. In the present study, we identified molecular mechanisms that are linked to the MuRF1 inhibition mediated protection against DIDD in rats. Briefly, MuRF1 inhibition upregulated pathways associated with: 1) muscle fiber structure and contractile function; 2) antioxidant defense; 3) chaperone-mediated unfolded protein response; 4) muscle cell growth, while downregulated pathways linked to 5) intramuscular lipid accumulation and 6) ECM collagen deposition.

Disrupted calcium homeostasis is reported to contribute to DIDD as evidenced by downregulation of key genes like SERCA1, impaired RyR1 activity, decreased Ca2+ sensitivity, and sarcoplasmic reticulum (SR) calcium leakage [6,26]. Consistent with

these findings, we observed a rapid downregulation of key genes involved in calcium handling, alongside increased phospholamban protein levels, a negative regulator of SERCA activity. MuRF1 has been reported to directly target proteins involved in calcium handling and muscle contraction [15–17]. Interestingly, MuRF1 inhibition prevented disuse-induced phospholamban elevation while upregulating S100A1 gene expression, although its protein levels remained unchanged. S100A1 is a calcium-binding protein that enhances RyR1 and SERCA activity, thus improving excitation-contraction coupling in striated muscles [27]. Moreover, S100A1 overexpression has been shown to rescue cardiac function throughout enhanced Ca^{2+} handling and myofibrillar protein Ca^{2+} responsiveness in heart failure models [28]. These findings suggest that MuRF1 inhibition may partially preserve calcium handling homeostasis via upregulation of S100A1 and blockade of phospholamban, likely contributing to preserved diaphragm contractile function during prolonged disuse.

Myofibrillar protein damage and post-translational modifications (PTMs) also contribute to early DIDD. ROS-induced oxidative modifications of myofibrillar proteins that impair muscle force-generation capacity have been detected as early as 6-12 hours following mechanical unloading [15–17]. Consistent with this, our data revealed rapid downregulation of genes critical for mitochondrial function, leading to augmented ROS production (i.e., oxidative stress) pathway. MuRF1 can directly regulate certain mitochondrial proteins [15–17]. Here, MuRF1 inhibition increased the mRNA levels of key antioxidant transcription factors (e.g., Nrf1, Nfe2l2) and enzymes (e.g., Sod2, Prdx1, Prdx6, and Gclc). These findings suggest that MuRF1 inhibition may improve antioxidant defense mechanisms, likely protecting diaphragm muscle fiber structure and contractile function under disuse stress.

Stress-induced unfolded protein response (UPR) activation contributes to maintaining muscle homeostasis under various stress states. Elevated oxidative stress and proteolysis contribute to myofibrillar protein damage, loss, and muscle wasting [7,29]. In addition, disuse induces diaphragm ultrastructural changes characterized by misaligned sarcomeres and impaired Z-disk [30], in part resulting from Z-disk-anchored titin loss [31]. Accordingly, we observed increased UPR pathway activation, which indicates a cellular response against myofibrillar protein damage and loss following 12 hours of mechanical unloading. Interestingly, MuRF1 inhibition significantly enhanced UPR pathway activation by upregulating transcription factors (e.g., XBP1, ATF4) that regulate co-chaperone (e.g., Bag3) and chaperone complexes (e.g., Cryab, Hspa5, Hspa8, Hspb8, Hsp90b1, Dnjb11, Cct5, etc.). Moreover, MuRF1 inhibition upregulated the expression of genes involved in sarcomere integrity maintenance. In this context, Bag3 facilitates chaperone-assisted selective autophagy (CASA) for myofibrillar protein maintenance, and its downregulation impairs contractile function and protein turnover [32]. Bag3 can also interact with alpha B-crystallin (i.e., Cryab) to regulate I-band and Z-disk integrity, while its regulation of Hsp70 chaperone activity protects against damaged protein aggregates and muscle homeostasis [33]. Similarly, chaperone co-inducer BGP-15 attenuates ventilation-induced diaphragmatic dysfunction by activating Hsp72 and reducing myosin post-translational modifications [34]. These findings indicate enhanced UPR and chaperone activation are key mechanisms underlying MuRF1 inhibition's protective effects against early DIDD.

It is well known that muscle mass regulation crucially depends on the balance between protein synthesis and degradation. After 12 h of disuse, we observed diaphragm

muscle atrophy across all fiber types, suggesting a catabolic shift. Nevertheless, we simultaneously observed increased expression of genes linked to muscle growth pathways (e.g., Myc, MAPK/ERK, and mTORC1) were upregulated, suggesting the activation of compensatory mechanisms to counteract muscle catabolism. Importantly, MuRF1 inhibition prevented disuse-induced diaphragm fiber atrophy and enhanced gene expression of pathways associated with RNA processing, ribosome biogenesis, protein synthesis, and cell growth (e.g., Myc, Nr4a3, PI3K-Akt-mTOR, eIF4e), which is consistent with the evidences that MuRF1 can directly target ribosomal components and translation factors [15–17].

We previously reported that MuRF1 inhibition increases Akt activation in the diaphragm under disuse stress [25]. In this study, we further confirm MuRF1 inhibition mediated activation of Akt-mTOR pathway during early DIDD. In accordance with this, MuRF1 knockout mice show enhanced Akt activation [24] and *de novo* protein synthesis, being less susceptible to muscle wasting [35]. Furthermore, MuRF1 may indirectly influence Myc activity by targeting Bin1, a negative Myc regulator [17]. Additionally, MuRF1 inhibition increased NR4A3 gene expression, which positively regulates mTORC1 signaling and has been shown to contribute to exercise-induced muscle hypertrophy [36]. Therefore, MuRF1 inhibition appears to activates anabolic pathways, thereby counteracting diaphragm fiber atrophy following prolonged disuse.

Increased protein damage and breakdown contribute to skeletal muscle wasting. Consistent with previous studies [9–11], we observed that prolonged disuse significantly upregulated inflammatory and proteolytic pathways (e.g., IL6-JAK-STAT3, TNFα/NFκB, ubiquitin-proteasome system) in the diaphragm. Unexpectedly,

animals treated with the MuRF1 inhibitor revealed a tendency (non-significant) to show relatively higher gene expression of MuRF1 (TRIM63) compared with DNV_VEH, without affecting protein levels, suggesting a compensatory cellular response attempting to enhance MuRF1 expression following disuse. These findings underscore the importance of dose-response optimization, as excessive MuRF1 inhibition may disrupt muscle homeostasis, as we previously reported [25]. Conversely, we observed that MuRF2 protein levels increased following disuse, a response abrogated by MuRF1 inhibition. This aligns with previous works supporting that MuRF1 deletion/inhibition can downregulate MuRF2 expression, and that MyoMed-205 can also inhibit MuRF2 [20], impairing MuRF1-MuRF2 heterodimerization, and consequently decreasing its cooperative role in myofibrillar protein ubiquitination [21,25,37]. Collectively, these findings suggest that MuRF1 inhibition may protect against early DIDD by disrupting MuRF1 activity and its cooperative interaction with MuRF2 in controlling myofibrillar breakdown.

Sustained cellular stress triggers myofiber apoptosis and diaphragm tissue remodeling, including intramuscular fat accumulation and fibrosis. Disuse rapidly induces intramuscular lipid accumulation in both rodent and human diaphragm [5,38]. Accordingly, we observed upregulated adipogenic gene expression and elevated ORO+ muscle cells containing increased intracellular lipid content after 12 h of disuse. MuRF1 inhibition alleviated these effects, likely through downregulation of key adipogenic genes (e.g., Adiponectin, Pparγ), potentially via inhibition/blockade of MuRF2, which is known to suppress Pparγ expression/activity [39]. Furthermore, prolonged disuse also enhanced gene expression linked to ECM collagen deposition and fibrosis, consistent with previous reports [40]. Notably, MuRF1 inhibition

prevented the disuse-induced ECM collagen deposition transcriptional response. Previous studies also demonstrated that MuRF1 inhibition mitigates cardiac fibrosis and improves contractile function during heart failure in rodents [22]. Collectively, these findings suggest that MuRF1 inhibition may contribute to the structural preservation of the diaphragm by mitigating intramuscular lipid accumulation and fibrosis, further supporting its therapeutic potential against DIDD.

Study Limitations

This is the first study to provide mechanistic insights into how the small-molecule inhibition of MuRF1 protects against early disuse-induced diaphragmatic dysfunction and atrophy in an experimental model. However, the following study limitations must be considered: 1) Our mechanistic findings are essentially supported by transcriptomic and protein content analyses, which do not take into account other important regulatory mechanisms, such as post-transcriptional and post-translational modifications, or changes in protein activity. Thus, future multi-omics analysis is warranted to further comprehend the complex molecular mechanisms underlying MuRF1 inhibition-mediated protection against early DIDD. 2) At this time, it was not possible to carry out cause-effect experiments to further validate which mechanisms are crucial for MuRF1 inhibition-mediated protection against early DIDD. 3) Although the small-molecule inhibition of MuRF1 seems an effective strategy to counteract DIDD secondary to phrenic nerve injury, further investigations are required to investigate whether MuRF1 inhibition can also counteract DIDD secondary to prolonged mechanical ventilation, which represents another clinically prevalent cause of DIDD in patients.

Conclusion

Small-molecule inhibition of MuRF1 protects against disuse-induced diaphragmatic dysfunction in rats undergoing 12 hours of UDD. Mechanistically, MuRF1 inhibition enhances the expression of genes associated with sarcomere structure and function, antioxidant defense, chaperone-mediated unfolded protein response, and pathways controlling muscle cell growth. Moreover, MuRF1 inhibition downregulated the expression of genes linked to intramuscular lipid accumulation and fibrosis. Overall, our findings suggest MuRF1 represents a promising therapeutic target to counteract early disuse-induced diaphragmatic dysfunction.

Author's Contributions

FR and ASM were involved in the study's conceptualization. FR conducted animal experiments, sample collection, functional, morphometric, and molecular analysis. PRJ conducted bioinformatic analysis (RNA-sequencing). FR and ASM performed data management and analysis. FR and ASM prepared the original manuscript. ASM and SL were involved in acquiring funding and project supervision. All authors were involved in the critical revision of the manuscript. All authors read and approved the final manuscript.

Acknowledgments

We wish to thank Kelly Patricia for her excellent laboratory technical assistance.

Funding

FR was supported by the São Paulo Research Foundation (FAPESP, grants 2020/04607-0 and 2022/14495-0). ASM was supported by FAPESP (grant 2022/16226-7) and the National Council for Scientific and Technological Development (CNPq, grant 305494/2022-8). PRJ was supported by Karolinska Institutet (KI) Research Foundation Grant. SL was supported by the German Centre for Cardiovascular Research (DZHK) partner site Mannheim-Heidelberg (grant SE-B42).

Ethical Standards Declaration

All animal studies have been approved by the appropriate ethics committee (CEUA ICB USP protocols #8728030320 and #5143091020), and have therefore been performed following the ethical standards laid down in the 1964 Declaration of Helsinki and its later amendments.

Conflict of Interest

Siegfried Labeit reports a patent filing for MyoMed-205 and further derivatives for its application to chronic muscle stress states (patent accession No WO2021023643A1). All other authors (Fernando Ribeiro, Paulo R. Jannig, and Anselmo S. Moriscot) declare no conflict of interest.

References

1. Fogarty MJ, Mantilla CB, Sieck GC. Breathing: Motor Control of Diaphragm Muscle. *Physiology* 2018;**33**:113–126.
2. McCool FD, Tzelepis GE. Dysfunction of the Diaphragm. *N Engl J Med* 2012;**366**:932–942.
3. van der Pijl R, Strom J, Conijn S, Lindqvist J, Labeit S, Granzier H *et al.* Titin-based mechanosensing modulates muscle hypertrophy. *J Cachexia Sarcopenia Muscle* 2018;**9**:947–961.
4. Ottenheijm CAC, van Hees HWH, Heunks LMA, Granzier H. Titin-based mechanosensing and signaling: role in diaphragm atrophy during unloading? *Am J Physiol Cell Mol Physiol* 2011;**300**:L161–L166.
5. Corpeno R, Dworkin B, Cacciani N, Salah H, Bergman H-M, Ravara B *et al.* Time course analysis of mechanical ventilation-induced diaphragm contractile muscle dysfunction in the rat. *J Physiol* 2014;**592**:3859–3880.
6. Ochala J, Radell PJ, Eriksson LI, Larsson L. EMD 57033 partially reverses ventilator-induced diaphragm muscle fibre calcium desensitisation. *Pflugers Arch Eur J Physiol* 2010;**459**:475–483.
7. Shanely RA, Zergeroglu MA, Lennon SL, Sugiura T, Yimlamai T, Enns D *et al.* Mechanical ventilation–induced diaphragmatic atrophy Is associated with oxidative injury and increased proteolytic activity. *Am J Respir Crit Care Med* 2002;**166**:1369–1374.
8. Ribeiro F, Zhang X, Wen Y, Cacciani N, Hedström Y, Xia Z *et al.* The role of zinc and matrix metalloproteinases in myofibrillar protein degradation in critical illness myopathy. *Free Radic Biol Med* 2024;**222**:493–504.
9. Argadine HM, Hellyer NJ, Mantilla CB, Zhan WZ, Sieck GC. The effect of denervation on protein synthesis and degradation in adult rat diaphragm muscle. *J Appl Physiol* 2009;**107**:438–444.
10. Hooijman PE, Beishuizen A, Witt CC, de Waard MC, Girbes ARJ, Spoelstra-de Man AME *et al.* Diaphragm muscle fiber weakness and ubiquitin–proteasome activation in critically ill patients. *Am J Respir Crit Care Med* 2015;**191**:1126–1138.
11. Hussain SNA, Mofarrahi M, Sigala I, Kim HC, Vassilakopoulos T, Maltais F *et al.* Mechanical Ventilation–induced Diaphragm Disuse in Humans Triggers Autophagy. *Am J Respir Crit Care Med* 2010;**182**:1377–1386.
12. Yang L, Luo J, Bourdon J, Lin MC, Gottfried SB, Petrof BJ. Controlled mechanical ventilation leads to remodeling of the rat diaphragm. *Am J Respir Crit Care Med* 2002;**166**:1135–1140.
13. Centner T, Yano J, Kimura E, McElhinny AS, Pelin K, Witt CC *et al.* Identification of muscle specific ring finger proteins as potential regulators of the titin kinase domain. *J Mol Biol* 2001;**306**:717–726.
14. Bodine SC, Latres E, Baumhueter S, Lai VK-M, Clarke BA, Poueymirou WT *et al.* Identification of ubiquitin ligases required for skeletal muscle atrophy. *Science (80-)* 2001;**294**:1704–1708.
15. Witt SH, Granzier H, Witt CC, Labeit S. MURF-1 and MURF-2 target a specific subset of myofibrillar proteins redundantly: Towards understanding MURF-dependent muscle ubiquitination. *J Mol Biol* 2005;**350**:713–722.
16. Witt CC, Witt SH, Lerche S, Labeit D, Back W, Labeit S. Cooperative control of striated muscle mass and metabolism by MuRF1 and MuRF2. *EMBO J* 2008;**27**:350–360.
17. Baehr LM, Hughes DC, Lynch SA, Van Haver D, Maia TM, Marshall AG *et al.* Identification of the MuRF1 Skeletal Muscle Ubiquitylome Through Quantitative Proteomics. *Function* 2021;**2**:1–18.
18. Peris-Moreno D, Taillandier D, Polge C. MuRF1/TRIM63, Master Regulator of Muscle Mass. *Int J Mol Sci* 2020;**21**:6663.

19. Liu J, Chen Y, Han D, Huang M. Inhibition of the expression of TRIM63 alleviates ventilator-induced diaphragmatic dysfunction by modulating the PPARα/PGC-1α pathway. *Mitochondrion* 2025;**83**:102025.
20. Bowen TS, Adams V, Werner S, Fischer T, Vinke P, Brogger MN *et al.* Small-molecule inhibition of MuRF1 attenuates skeletal muscle atrophy and dysfunction in cardiac cachexia. *J Cachexia Sarcopenia Muscle* 2017;**8**:939–953.
21. Adams V, Bowen TS, Werner S, Barthel P, Amberger C, Konzer A *et al.* Small-molecule-mediated chemical knock-down of MuRF1/MuRF2 and attenuation of diaphragm dysfunction in chronic heart failure. *J Cachexia Sarcopenia Muscle* 2019;**10**:1102–1115.
22. Adams V, Schauer A, Augstein A, Kirchhoff V, Draskowski R, Jannasch A *et al.* Targeting MuRF1 by small molecules in a HFpEF rat model improves myocardial diastolic function and skeletal muscle contractility. *J Cachexia Sarcopenia Muscle* 2022;**13**:1565–1581.
23. Adams V, Gußen V, Zozulya S, Cruz A, Moriscot A, Linke A *et al.* Small-Molecule Chemical Knockdown of MuRF1 in Melanoma Bearing Mice Attenuates Tumor Cachexia Associated Myopathy. *Cells* 2020;**9**:2272.
24. Labeit S, Hirner S, Bogomolovas J, Cruz A, Myrzabekova M, Moriscot A *et al.* Regulation of Glucose Metabolism by MuRF1 and Treatment of Myopathy in Diabetic Mice with Small Molecules Targeting MuRF1. *Int J Mol Sci* 2021;**22**:2225.
25. Ribeiro F, Alves PKN, Bechara LRG, Ferreira JCB, Labeit S, Moriscot AS. Small-Molecule Inhibition of MuRF1 Prevents Early Disuse-Induced Diaphragmatic Dysfunction and Atrophy. *Int J Mol Sci* 2023;**24**:3637.
26. Matecki S, Dridi H, Jung B, Saint N, Reiken SR, Scheuermann V *et al.* Leaky ryanodine receptors contribute to diaphragmatic weakness during mechanical ventilation. *Proc Natl Acad Sci U S A* 2016;**113**:9069–9074.
27. Kiewitz R, Acklin C, Schäfer BW, Maco B, Uhrík B, Wuytack F *et al.* Ca2+-dependent interaction of S100A1 with the sarcoplasmic reticulum Ca2+-ATPase2a and phospholamban in the human heart. *Biochem Biophys Res Commun* 2003;**306**:550–557.
28. Most P, Bernotat J, Ehlermann P, Pleger ST, Reppel M, Börries M *et al.* S100A1: A regulator of myocardial contractility. *Proc Natl Acad Sci* 2001;**98**:13889–13894.
29. Li S, Luo G, Zeng R, Lin L, Zou X, Yan Y *et al.* Endoplasmic Reticulum Stress Contributes to Ventilator-Induced Diaphragm Atrophy and Weakness in Rats. *Front Physiol* 2022;**13**:1–13.
30. Jaber S, Petrof BJ, Jung B, Chanques G, Berthet J-P, Rabuel C *et al.* Rapidly Progressive Diaphragmatic Weakness and Injury during Mechanical Ventilation in Humans. *Am J Respir Crit Care Med* 2011;**183**:364–371.
31. Swist S, Unger A, Li Y, Vöge A, von Frieling-Salewsky M, Skärlén Å *et al.* Maintenance of sarcomeric integrity in adult muscle cells crucially depends on Z-disc anchored titin. *Nat Commun* 2020;**11**:1–18.
32. Martin TG, Myers VD, Dubey P, Dubey S, Perez E, Moravec CS *et al.* Cardiomyocyte contractile impairment in heart failure results from reduced BAG3-mediated sarcomeric protein turnover. *Nat Commun* 2021;**12**:2942.
33. Meister-Broekema M, Freilich R, Jagadeesan C, Rauch JN, Bengoechea R, Motley WW *et al.* Myopathy associated BAG3 mutations lead to protein aggregation by stalling Hsp70 networks. *Nat Commun* 2018;**9**:5342.
34. Salah H, Li M, Cacciani N, Gastaldello S, Ogilvie H, Akkad H *et al.* The chaperone co-inducer BGP-15 alleviates ventilation-induced diaphragm dysfunction. *Sci Transl Med* 2016;**8**:350ra103.
35. Koyama S, Hata S, Witt CC, Ono Y, Lerche S, Ojima K *et al.* Muscle RING-Finger Protein-1 (MuRF1) as a connector of muscle energy metabolism and protein synthesis. *J Mol Biol* 2008;**376**:1224–1236.
36. Pillon NJ, Gabriel BM, Dollet L, Smith JAB, Sardón Puig L, Botella J *et al.* Transcriptomic profiling of skeletal muscle adaptations to exercise and inactivity. *Nat*

Commun 2020;**11**:470.
37. Nguyen T, Bowen TS, Augstein A, Schauer A, Gasch A, Linke A *et al.* Expression of MuRF1 or MuRF2 is essential for the induction of skeletal muscle atrophy and dysfunction in a murine pulmonary hypertension model. *Skelet Muscle* 2020;**10**:1–10.
38. Picard M, Jung B, Liang F, Azuelos I, Hussain S, Goldberg P *et al.* Mitochondrial dysfunction and lipid accumulation in the human diaphragm during mechanical ventilation. *Am J Respir Crit Care Med* 2012;**186**:1140–1149.
39. He J, Quintana MT, Sullivan J, L Parry T, J Grevengoed T, Schisler JC *et al.* MuRF2 regulates PPARγ1 activity to protect against diabetic cardiomyopathy and enhance weight gain induced by a high fat diet. *Cardiovasc Diabetol* 2015;**14**:97.
40. Qian X, Jiang Y, Jia J, Shen W, Ding Y, He Y *et al.* PEEP application during mechanical ventilation contributes to fibrosis in the diaphragm. *Respir Res* 2023;**24**:46.

Figure Legends

Figure 1. Transcriptomic profiling of the diaphragm following 12 h of mechanical unloading and identification of pathways responsive to MuRF1 inhibition. (A) Schematic illustration of the experimental design used to investigate the effect of small-molecule mediated inhibition of MuRF1 (MyoMed-205, 50 mg/kg bw, intravenous delivery) upon early disuse-induced diaphragmatic dysfunction (DIDD) pathophysiology induced by 12 h of UDD in rats. (B) Principal component analysis for RNA-seq of diaphragm muscle and identification of differentially expressed genes (DEGs, Padj < 0.05) across the distinct experimental conditions (*n* = 4 per group). Upregulated genes are represented in red, while downregulated genes are represented in blue. (C) Hierarchical clustered heat map highlights five clusters of DEGs identified in response to mechanical unloading and MuRF1 inhibition compared with the control. (D) Gene Set Enrichment Analysis (GSEA) reveals the hallmark pathways responsive to prolonged diaphragm disuse and the impacts of MuRF1 inhibition. Additionally, GSEA indicates the altered (E) molecular functions (GOMF) and (F) cellular compartments (GOCC) of the diaphragm muscle in response to mechanical unloading and MuRF1 inhibition compared with controls. Padj, adjusted p-value. FDR, false discovery rate.

Figure 2. MuRF1 inhibition protects against early disuse-induced diaphragmatic dysfunction. (A) Representative photomicrographs of diaphragm muscle immunolabeled with antibodies against the myosin heavy chain (MyHC) isoforms and dystrophin for morphometric analysis by fiber type. Scale bar = 100 μm. (B) Fibers' cross-sectional area (CSA) and relative percentual distribution. Data are presented as mean and standard deviation (*n* = 8). One-way ANOVA followed by Tukey's post-hoc

test was used for statistical comparisons among the groups. *, $p < 0.05$. (C) Heat map of genes linked to muscle contraction (i.e., synaptic vesicle membrane and contractile file). (D) Heat map of genes linked to sarcomere structure and function (i.e., actin filament, I band, and dystrophin glycoprotein complex (DCG)). (F) Protein levels of calcium-handling markers were assessed by Western blotting. Data are presented as mean and standard deviation of the fold change relative to the control group (n = 7 to 8). One-way ANOVA followed by Tukey's post-hoc test was used for statistical comparisons among the groups. *, $p < 0.05$.

Figure 3. Disuse promotes mitochondrial dysfunction and oxidative stress, while inhibition of MuRF1 enhances the expression of antioxidant genes. (A) Heat map of genes involved in the control of mitochondrial biogenesis and dynamics. (B-C) Heat map of genes associated with mitochondrial structural and functional complexes. (D) Heat map of genes linked to mitochondrial energy production and metabolism. (E) Heat map of genes involved with reactive oxygen species (ROS) production and antioxidant response.

Figure 4. MuRF1 inhibition enhances the activation of signaling pathways controlling ribosome biogenesis, protein synthesis and cell growth. (A) Heat map of Myc target genes. (B) Heat map of genes associated with the PI3K-AKT-mTOR pathway. (C) Heat map of genes controlling ribosome biogenesis and translation initiation. (D) Protein levels of MAPK and PI3K-Akt-mTOR pathways markers were assessed by Western blotting. Data are presented as mean and standard deviation of the fold change relative to the control group (n = 6 to 7). One-way ANOVA followed by Tukey's

post-hoc test was used for statistical comparisons among the groups. *, $p < 0.05$; **, $p < 0.01$.

Figure 5. MuRF1 inhibition enhances the expression of heat shock chaperones and improves the unfolded protein response during cell stress and catabolism states. (A) Heat map of genes from the IL6-JAK-STAT3 pathway. (B) Heat map of genes associated with chaperone complex and unfolded protein response. (C) Heat map of genes linked to the ubiquitin-proteasome system. (D) Protein levels of ubiquitin-proteasome pathway markers were assessed by Western blotting. Data are presented as mean and standard deviation of the fold change relative to the control group (n = 8). One-way ANOVA followed by Tukey's post-hoc test was used for statistical comparisons among the groups. *, $p < 0.05$; **, $p < 0.01$. (E) Heat maps of genes from the p53 pathway. (F) Heat maps of genes associated with apoptosis.

Figure 6. MuRF1 inhibition attenuates disuse-induced intramuscular fat accumulation in the diaphragm by downregulating pro-adipogenic genes. (A) Heat map of genes related to adipogenesis and intramuscular lipid accumulation. (B) Protein levels of adipogenesis pathway markers were assessed by Western blotting. Data are presented as mean and standard deviation of the fold change relative to the control group (n = 8). One-way ANOVA followed by Tukey's post-hoc test was used for statistical comparisons among the groups. (C) Representative photomicrographs of Oil Red O (ORO) staining of the diaphragm for assessing intramuscular lipid accumulation following 12 h of disuse and the impacts of MuRF1 inhibition. Scale bar = 50 μm. (D) Quantitative analysis of positive ORO muscle cells (i.e., intracellular lipid droplet area > 5% of total muscle fiber area). (E) Mean intracellular lipid droplet area

of diaphragm muscle fibers < 2500 μm^2 (predominantly oxidative metabolism) and fibers > 2500 μm^2 (predominantly glycolytic metabolism). In total, 300 muscle cells were assessed per sample to estimate the average positive ORO cells and intracellular lipid content. Data are presented as mean and standard deviation (n = 7). One-way ANOVA followed by Tukey's post-hoc test was used for statistical comparisons among the groups. *, $p < 0.05$; **, $p < 0.01$.

Figure 7. MuRF1 inhibition prevented the disuse-induced upregulation of genes involved with extracellular matrix collagen deposition and fibrosis in the diaphragm. (A) Heat map of genes involved in the formation of collagen trimmers. (B) Heat map of genes associated with the basement membrane. (C) Heat map of genes associated with collagen assembly and the extracellular matrix.

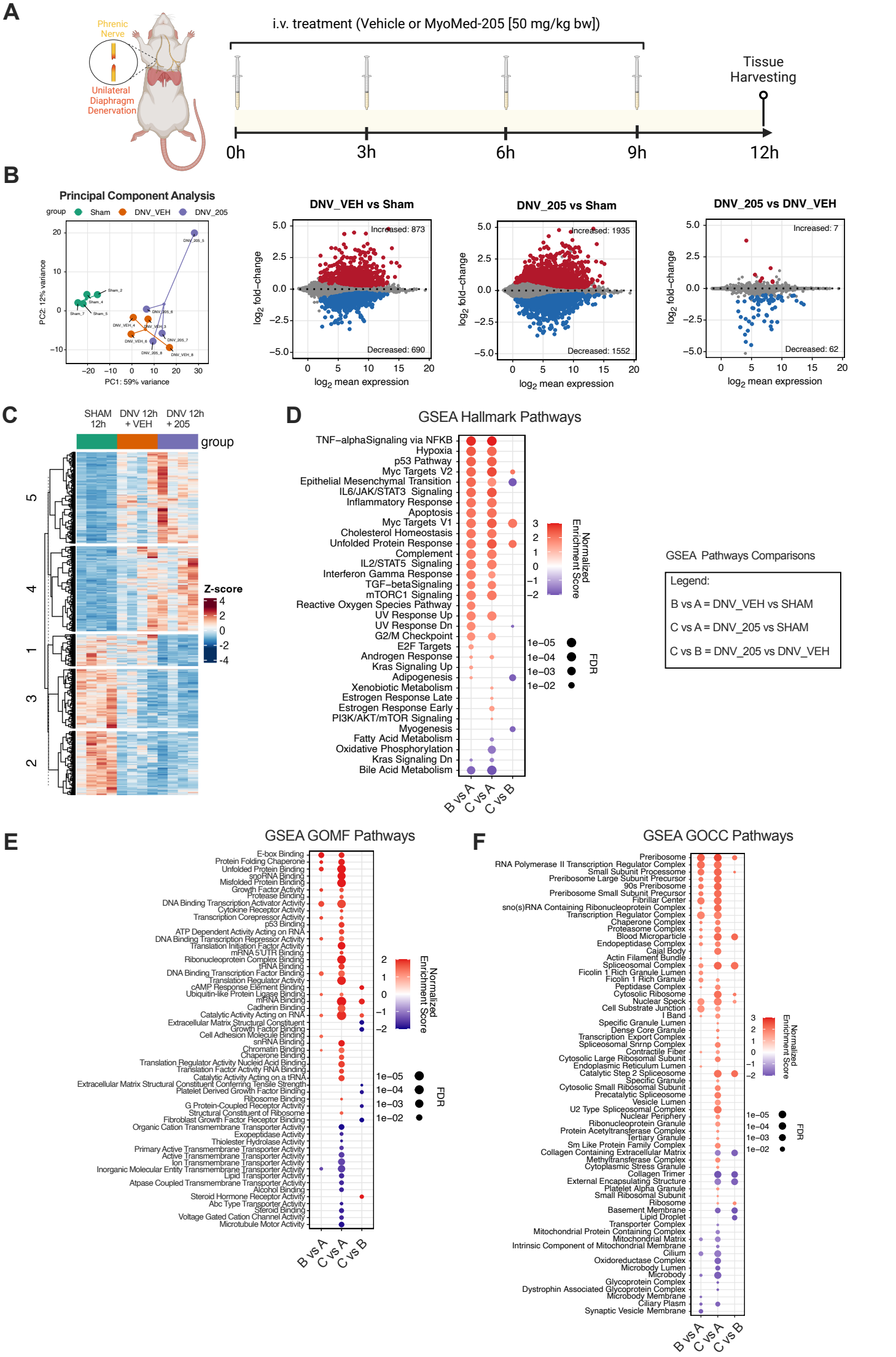
A
Phrenic Nerve
Unilateral Diaphragm Denervation
i.v. treatment (Vehicle or MyoMed-205 [50 mg/kg bw])
Tissue Harvesting
0h
3h
6h
9h
12h
B
Principal Component Analysis
group Sham DNV_VEH DNV_205
PC2: 12% variance
PC1: 59% variance
DNV_VEH vs Sham
Increased: 873
Decreased: 690
DNV_205 vs Sham
Increased: 1935
Decreased: 1552
DNV_205 vs DNV_VEH
Increased: 7
Decreased: 62
log2 fold-change
log2 mean expression
C
SHAM 12h
DNV 12h + VEH
DNV 12h + 205
group
Z-score
D
GSEA Hallmark Pathways
TNF-alphaSignaling via NFKB
Hypoxia
p53 Pathway
Myc Targets V2
Epithelial Mesenchymal Transition
IL6/JAK/STAT3 Signaling
Inflammatory Response
Apoptosis
Myc Targets V1
Cholesterol Homeostasis
Unfolded Protein Response
Complement
IL2/STAT5 Signaling
Interferon Gamma Response
TGF-betaSignaling
mTORC1 Signaling
Reactive Oxygen Species Pathway
UV Response Up
UV Response Dn
G2/M Checkpoint
E2F Targets
Androgen Response
Kras Signaling Up
Adipogenesis
Xenobiotic Metabolism
Estrogen Response Late
Estrogen Response Early
PI3K/AKT/mTOR Signaling
Myogenesis
Fatty Acid Metabolism
Oxidative Phosphorylation
Kras Signaling Dn
Bile Acid Metabolism
B vs A
C vs A
C vs B
Normalized Enrichment Score
FDR
GSEA Pathways Comparisons
Legend:
B vs A = DNV_VEH vs SHAM
C vs A = DNV_205 vs SHAM
C vs B = DNV_205 vs DNV_VEH
E
GSEA GOMF Pathways
F
GSEA GOCC Pathways

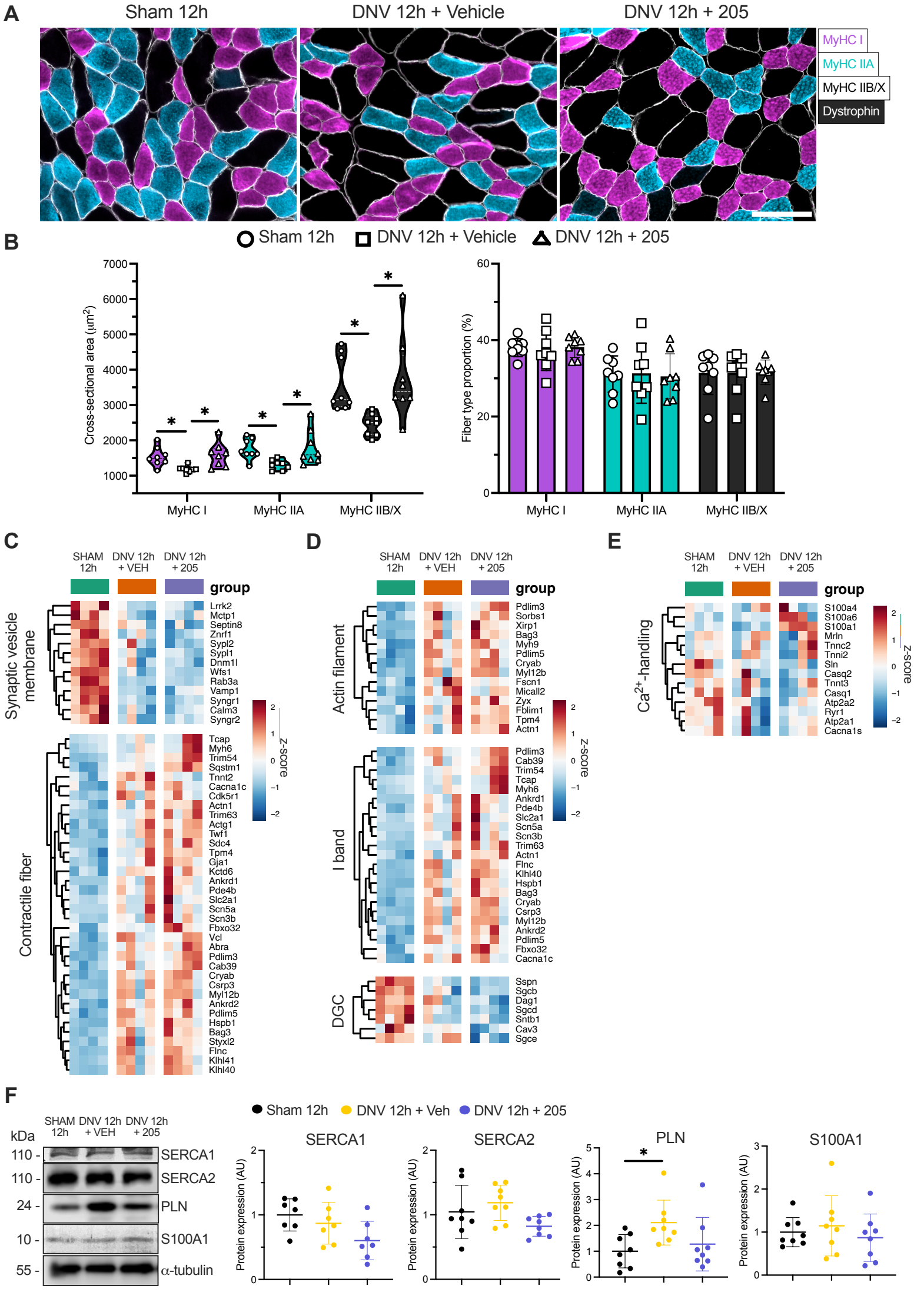
A
Sham 12h
DNV 12h + Vehicle
DNV 12h + 205
MyHC I
MyHC IIA
MyHC IIB/X
Dystrophin
B
Sham 12h
DNV 12h + Vehicle
DNV 12h + 205
Cross-sectional area (μm²)
Fiber type proportion (%)
MyHC I
MyHC IIA
MyHC IIB/X
C
SHAM 12h
DNV 12h + VEH
DNV 12h + 205
group
Synaptic vesicle membrane
Contractile fiber
z-score
D
Actin filament
I band
DGC
E
Ca2+-handling
F
kDa
SERCA1
SERCA2
PLN
S100A1
α-tubulin
Sham 12h
DNV 12h + Veh
DNV 12h + 205
Protein expression (AU)

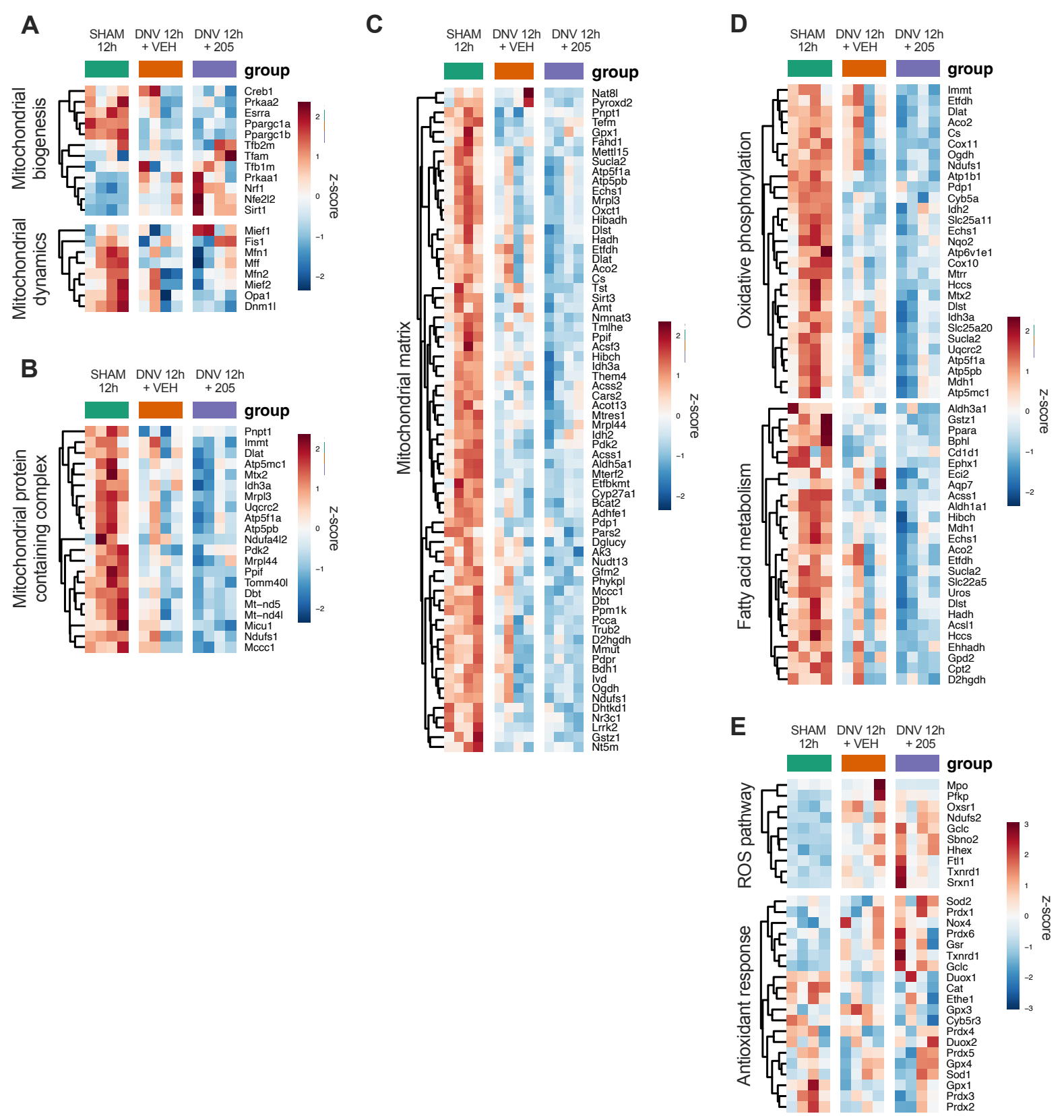
A
SHAM 12h
DNV 12h + VEH
DNV 12h + 205
group
Mitochondrial biogenesis
Creb1
Prkaa2
Esrra
Ppargc1a
Ppargc1b
Tfb2m
Tfam
Tfb1m
Prkaa1
Nrf1
Nfe2l2
Sirt1
Mitochondrial dynamics
Mief1
Fis1
Mfn1
Mff
Mfn2
Mief2
Opa1
Dnm1l
z-score
2
1
0
−1
−2
B
SHAM 12h
DNV 12h + VEH
DNV 12h + 205
group
Mitochondrial protein containing complex
Pnpt1
Immt
Dlat
Atp5mc1
Mtx2
Idh3a
Mrpl3
Uqcrc2
Atp5f1a
Atp5pb
Ndufa4l2
Pdk2
Mrpl44
Ppif
Tomm40l
Dbt
Mt−nd5
Mt−nd4l
Micu1
Ndufs1
Mccc1
z-score
2
1
0
−1
−2
C
SHAM 12h
DNV 12h + VEH
DNV 12h + 205
group
Mitochondrial matrix
Nat8l
Pyroxd2
Pnpt1
Tefm
Gpx1
Fahd1
Mettl15
Sucla2
Atp5f1a
Atp5pb
Echs1
Mrpl3
Oxct1
Hibadh
Dlst
Hadh
Etfdh
Dlat
Aco2
Cs
Tst
Sirt3
Amt
Nmnat3
Tmlhe
Ppif
Acsf3
Hibch
Idh3a
Them4
Acss2
Cars2
Acot13
Mtres1
Mrpl44
Idh2
Pdk2
Acss1
Aldh5a1
Mterf2
Etfbkmt
Cyp27a1
Bcat2
Adhfe1
Pdp1
Pars2
Dglucy
Ak3
Nudt13
Gfm2
Phykpl
Mccc1
Dbt
Ppm1k
Pcca
Trub2
D2hgdh
Mmut
Pdpr
Bdh1
Ivd
Ogdh
Ndufs1
Dhtkd1
Nr3c1
Lrrk2
Gstz1
Nt5m
z-score
2
1
0
−1
−2
D
SHAM 12h
DNV 12h + VEH
DNV 12h + 205
group
Oxidative phosphorylation
Immt
Etfdh
Dlat
Aco2
Cs
Cox11
Ogdh
Ndufs1
Atp1b1
Pdp1
Cyb5a
Idh2
Slc25a11
Echs1
Nqo2
Atp6v1e1
Cox10
Mtrr
Hccs
Mtx2
Dlst
Idh3a
Slc25a20
Sucla2
Uqcrc2
Atp5f1a
Atp5pb
Mdh1
Atp5mc1
Fatty acid metabolism
Aldh3a1
Gstz1
Ppara
Bphl
Cd1d1
Ephx1
Eci2
Aqp7
Acss1
Aldh1a1
Hibch
Mdh1
Echs1
Aco2
Etfdh
Sucla2
Slc22a5
Uros
Dlst
Hadh
Acsl1
Hccs
Ehhadh
Gpd2
Cpt2
D2hgdh
z-score
2
1
0
−1
−2
E
SHAM 12h
DNV 12h + VEH
DNV 12h + 205
group
ROS pathway
Mpo
Pfkp
Oxsr1
Ndufs2
Gclc
Sbno2
Hhex
Ftl1
Txnrd1
Srxn1
Antioxidant response
Sod2
Prdx1
Nox4
Prdx6
Gsr
Txnrd1
Gclc
Duox1
Cat
Ethe1
Gpx3
Cyb5r3
Prdx4
Duox2
Prdx5
Gpx4
Sod1
Gpx1
Prdx3
Prdx2
z-score
3
2
1
0
−1
−2
−3

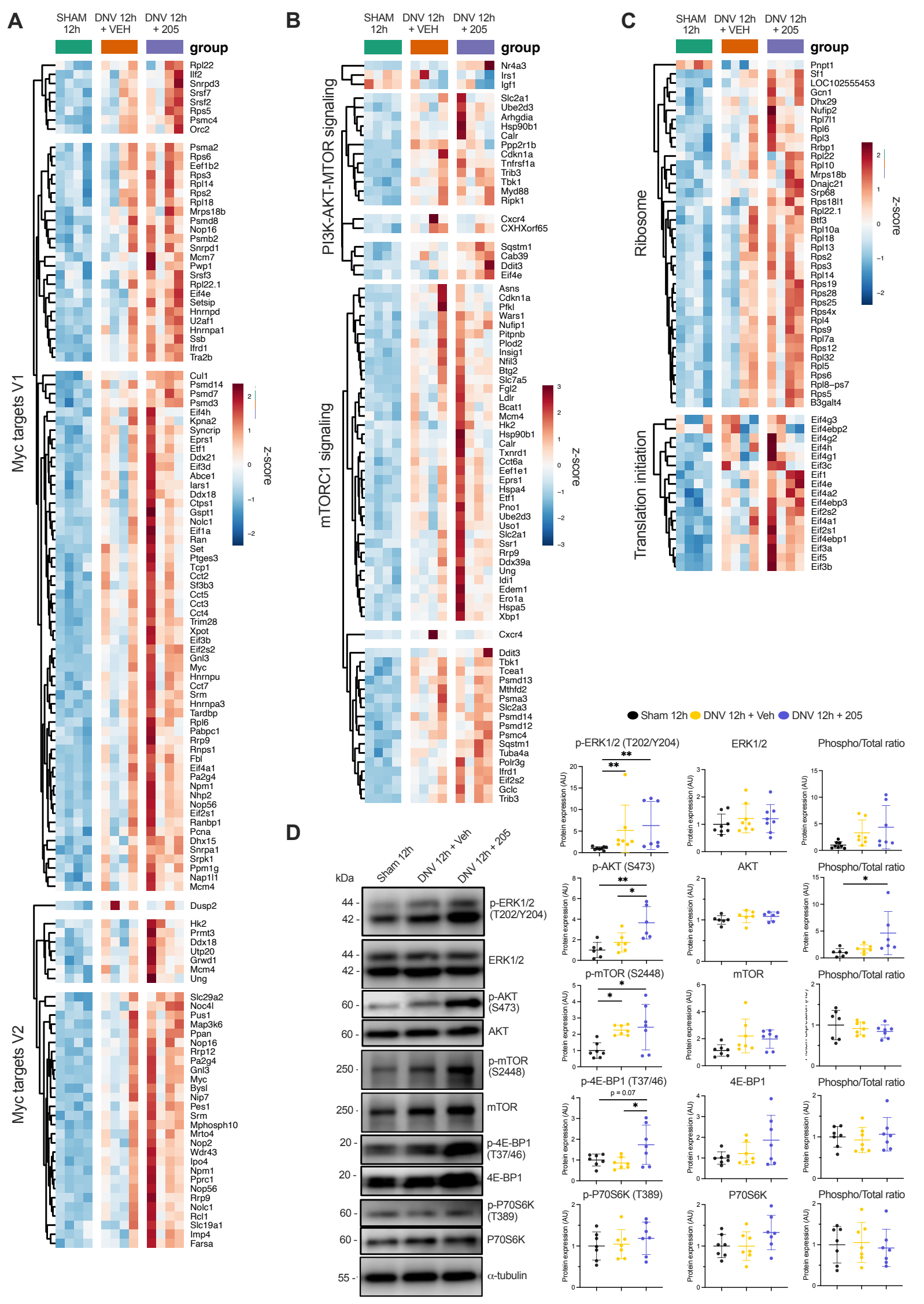
A
SHAM 12h
DNV 12h + VEH
DNV 12h + 205
group
Myc targets V1
Rpl22
Ilf2
Snrpd3
Srsf7
Srsf2
Rps5
Psmc4
Orc2
Psma2
Rps6
Eef1b2
Rps3
Rpl14
Rps2
Rpl18
Mrps18b
Psmd8
Nop16
Psmb2
Snrpd1
Mcm7
Pwp1
Srsf3
Rpl22.1
Eif4e
Setsip
Hnrnpd
U2af1
Hnrnpa1
Ssb
Ifrd1
Tra2b
Cul1
Psmd14
Psmd7
Psmd3
Eif4h
Kpna2
Syncrip
Eprs1
Etf1
Ddx21
Eif3d
Abce1
Iars1
Ddx18
Ctps1
Gspt1
Nolc1
Eif1a
Ran
Set
Ptges3
Tcp1
Cct2
Sf3b3
Cct5
Cct3
Cct4
Trim28
Xpot
Eif3b
Eif2s2
Gnl3
Myc
Hnrnpu
Cct7
Srm
Hnrnpa3
Tardbp
Rpl6
Pabpc1
Rrp9
Rnps1
Fbl
Eif4a1
Pa2g4
Npm1
Nhp2
Nop56
Eif2s1
Ranbp1
Pcna
Dhx15
Snrpa1
Srpk1
Ppm1g
Nap1l1
Mcm4
Dusp2
Myc targets V2
Hk2
Prmt3
Ddx18
Utp20
Grwd1
Mcm4
Ung
Slc29a2
Noc4l
Pus1
Map3k6
Ppan
Nop16
Rrp12
Pa2g4
Gnl3
Myc
Bysl
Nip7
Pes1
Srm
Mphosph10
Mrto4
Nop2
Wdr43
Ipo4
Npm1
Pprc1
Nop56
Rrp9
Nolc1
Rcl1
Slc19a1
Imp4
Farsa
z-score
B
PI3K-AKT-MTOR signaling
Nr4a3
Irs1
Igf1
Slc2a1
Ube2d3
Arhgdia
Hsp90b1
Calr
Ppp2r1b
Cdkn1a
Tnfrsf1a
Trib3
Tbk1
Myd88
Ripk1
Cxcr4
CXHXorf65
Sqstm1
Cab39
Ddit3
Eif4e
mTORC1 signaling
Asns
Cdkn1a
Pfkl
Wars1
Nufip1
Pitpnb
Plod2
Insig1
Nfil3
Btg2
Slc7a5
Fgl2
Ldlr
Bcat1
Mcm4
Hk2
Hsp90b1
Calr
Txnrd1
Cct6a
Eef1e1
Eprs1
Hspa4
Etf1
Pno1
Ube2d3
Uso1
Slc2a1
Ssr1
Rrp9
Ddx39a
Ung
Idi1
Edem1
Ero1a
Hspa5
Xbp1
Cxcr4
Ddit3
Tbk1
Tcea1
Psmd13
Mthfd2
Psma3
Slc2a3
Psmd14
Psmd12
Psmc4
Sqstm1
Tuba4a
Polr3g
Ifrd1
Eif2s2
Gclc
Trib3
z-score
C
Ribosome
Pnpt1
Sf1
LOC102555453
Gcn1
Dhx29
Nufip2
Rpl7l1
Rpl6
Rpl3
Rrbp1
Rpl22
Rpl10
Mrps18b
Dnajc21
Srp68
Rps18l1
Rpl22.1
Btf3
Rpl10a
Rpl18
Rpl13
Rps2
Rps3
Rpl14
Rps19
Rps28
Rps25
Rps4x
Rpl4
Rps9
Rpl7a
Rps12
Rpl32
Rpl5
Rps6
Rpl8–ps7
Rps5
B3galt4
Translation initiation
Eif4g3
Eif4ebp2
Eif4g2
Eif4h
Eif4g1
Eif3c
Eif1
Eif4e
Eif4a2
Eif4ebp3
Eif2s2
Eif4a1
Eif2s1
Eif4ebp1
Eif3a
Eif5
Eif3b
z-score
D
kDa
Sham 12h
DNV 12h + Veh
DNV 12h + 205
44
42
p-ERK1/2 (T202/Y204)
ERK1/2
60
p-AKT (S473)
AKT
250
p-mTOR (S2448)
mTOR
20
p-4E-BP1 (T37/46)
4E-BP1
p-P70S6K (T389)
P70S6K
55
α-tubulin
Sham 12h
DNV 12h + Veh
DNV 12h + 205
p-ERK1/2 (T202/Y204)
ERK1/2
Phospho/Total ratio
p-AKT (S473)
AKT
Phospho/Total ratio
p-mTOR (S2448)
mTOR
Phospho/Total ratio
p-4E-BP1 (T37/46)
p = 0.07
4E-BP1
Phospho/Total ratio
p-P70S6K (T389)
P70S6K
Phospho/Total ratio
Protein expression (AU)

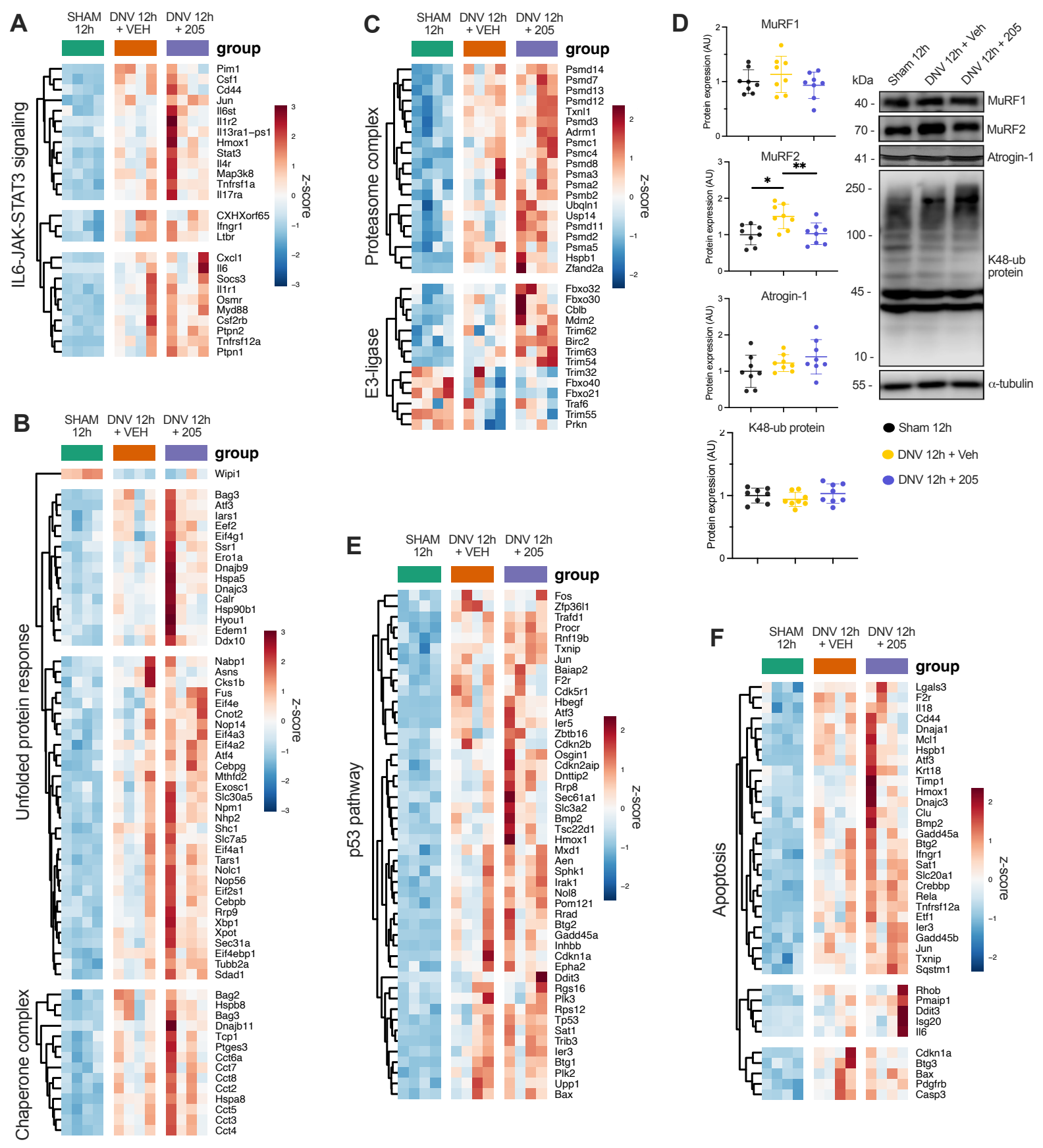
A
SHAM 12h
DNV 12h + VEH
DNV 12h + 205
group
IL6-JAK-STAT3 signaling
Pim1
Csf1
Cd44
Jun
Il6st
Il1r2
Il13ra1−ps1
Hmox1
Stat3
Il4r
Map3k8
Tnfrsf1a
Il17ra
CXHXorf65
Ifngr1
Ltbr
Cxcl1
Il6
Socs3
Il1r1
Osmr
Myd88
Csf2rb
Ptpn2
Tnfrsf12a
Ptpn1
z-score
B
Unfolded protein response
Wipi1
Bag3
Atf3
Iars1
Eef2
Eif4g1
Ssr1
Ero1a
Dnajb9
Hspa5
Dnajc3
Calr
Hsp90b1
Hyou1
Edem1
Ddx10
Nabp1
Asns
Cks1b
Fus
Eif4e
Cnot2
Nop14
Eif4a3
Eif4a2
Atf4
Cebpg
Mthfd2
Exosc1
Slc30a5
Npm1
Nhp2
Shc1
Slc7a5
Eif4a1
Tars1
Nolc1
Nop56
Eif2s1
Cebpb
Rrp9
Xbp1
Xpot
Sec31a
Eif4ebp1
Tubb2a
Sdad1
Chaperone complex
Bag2
Hspb8
Bag3
Dnajb11
Tcp1
Ptges3
Cct6a
Cct7
Cct8
Cct2
Hspa8
Cct5
Cct3
Cct4
C
Proteasome complex
Psmd14
Psmd7
Psmd13
Psmd12
Txnl1
Psmd3
Adrm1
Psmc1
Psmc4
Psmd8
Psma3
Psma2
Psmb2
Ubqln1
Usp14
Psmd11
Psmd2
Psma5
Hspb1
Zfand2a
E3-ligase
Fbxo32
Fbxo30
Cblb
Mdm2
Trim62
Birc2
Trim63
Trim54
Trim32
Fbxo40
Fbxo21
Traf6
Trim55
Prkn
D
MuRF1
MuRF2
Atrogin-1
K48-ub protein
Protein expression (AU)
kDa
Sham 12h
DNV 12h + Veh
DNV 12h + 205
40 -
70 -
41 -
250 -
100 -
45 -
10 -
55 -
α-tubulin
E
p53 pathway
Fos
Zfp36l1
Trafd1
Procr
Rnf19b
Txnip
Jun
Baiap2
F2r
Cdk5r1
Hbegf
Atf3
Ier5
Zbtb16
Cdkn2b
Osgin1
Cdkn2aip
Dnttip2
Rrp8
Sec61a1
Slc3a2
Bmp2
Tsc22d1
Hmox1
Mxd1
Aen
Sphk1
Irak1
Nol8
Pom121
Rrad
Btg2
Gadd45a
Inhbb
Cdkn1a
Epha2
Ddit3
Rgs16
Plk3
Rps12
Tp53
Sat1
Trib3
Ier3
Btg1
Plk2
Upp1
Bax
F
Apoptosis
Lgals3
F2r
Il18
Cd44
Dnaja1
Mcl1
Hspb1
Atf3
Krt18
Timp1
Hmox1
Dnajc3
Clu
Bmp2
Gadd45a
Btg2
Ifngr1
Sat1
Slc20a1
Crebbp
Rela
Tnfrsf12a
Etf1
Ier3
Gadd45b
Jun
Txnip
Sqstm1
Rhob
Pmaip1
Ddit3
Isg20
Il6
Cdkn1a
Btg3
Bax
Pdgfrb
Casp3

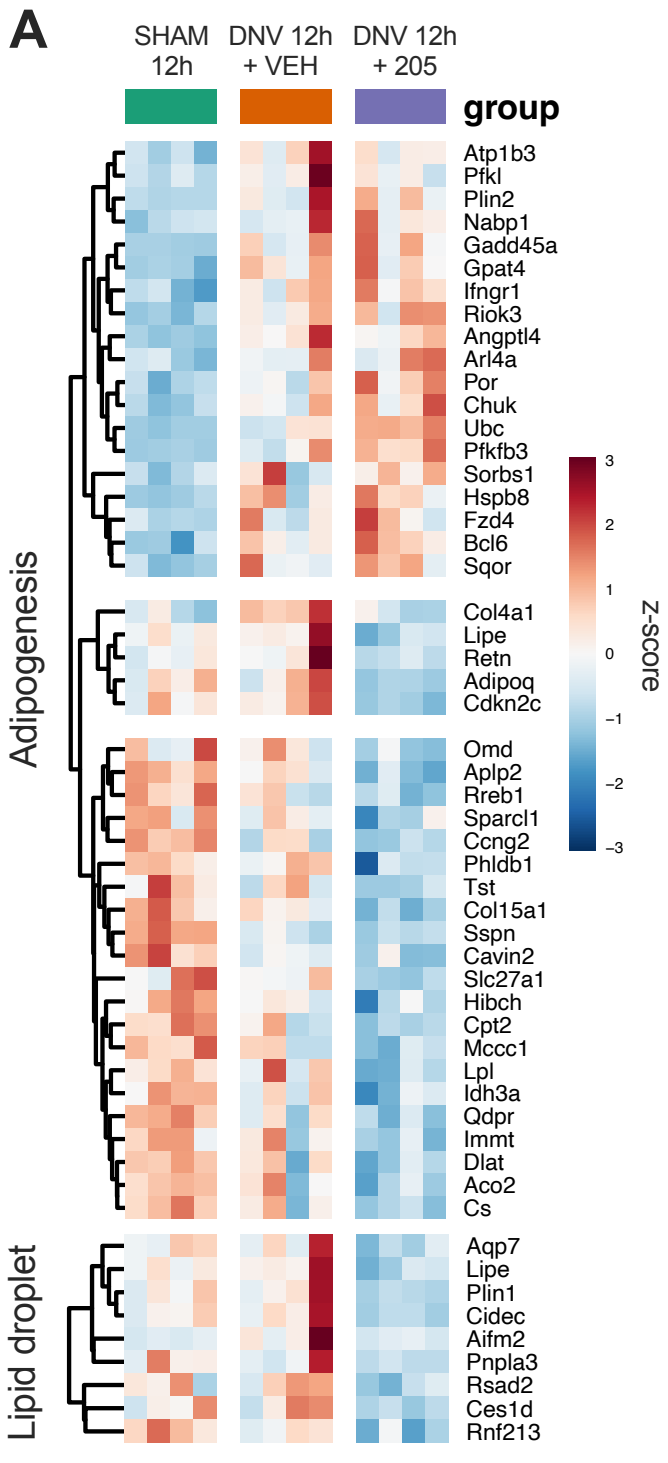
A
SHAM 12h
DNV 12h + VEH
DNV 12h + 205
group
Adipogenesis
Lipid droplet
Atp1b3
Pfkl
Plin2
Nabp1
Gadd45a
Gpat4
Ifngr1
Riok3
Angptl4
Arl4a
Por
Chuk
Ubc
Pfkfb3
Sorbs1
Hspb8
Fzd4
Bcl6
Sqor
Col4a1
Lipe
Retn
Adipoq
Cdkn2c
Omd
Aplp2
Rreb1
Sparcl1
Ccng2
Phldb1
Tst
Col15a1
Sspn
Cavin2
Slc27a1
Hibch
Cpt2
Mccc1
Lpl
Idh3a
Qdpr
Immt
Dlat
Aco2
Cs
Aqp7
Lipe
Plin1
Cidec
Aifm2
Pnpla3
Rsad2
Ces1d
Rnf213
Z-score
3
2
1
0
−1
−2
−3

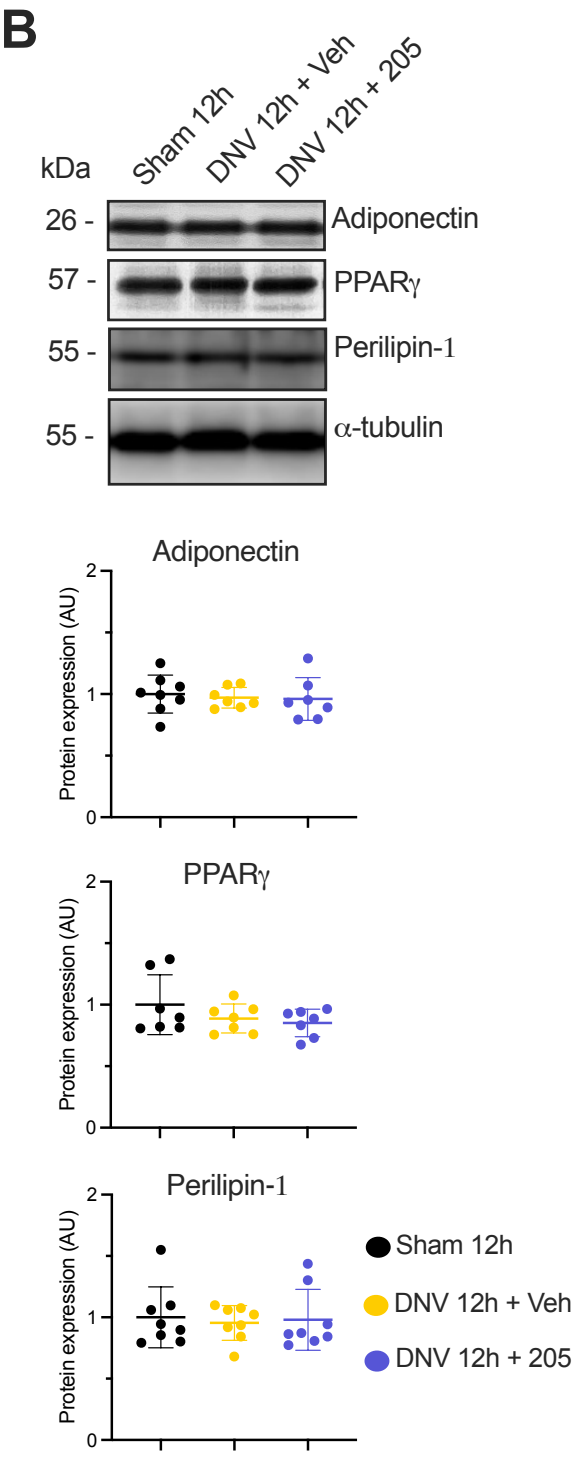
B
kDa
Sham 12h
DNV 12h + Veh
DNV 12h + 205
26 -
Adiponectin
57 -
PPARγ
55 -
Perilipin-1
55 -
α-tubulin
Adiponectin
PPARγ
Perilipin-1
Protein expression (AU)
Sham 12h
DNV 12h + Veh
DNV 12h + 205

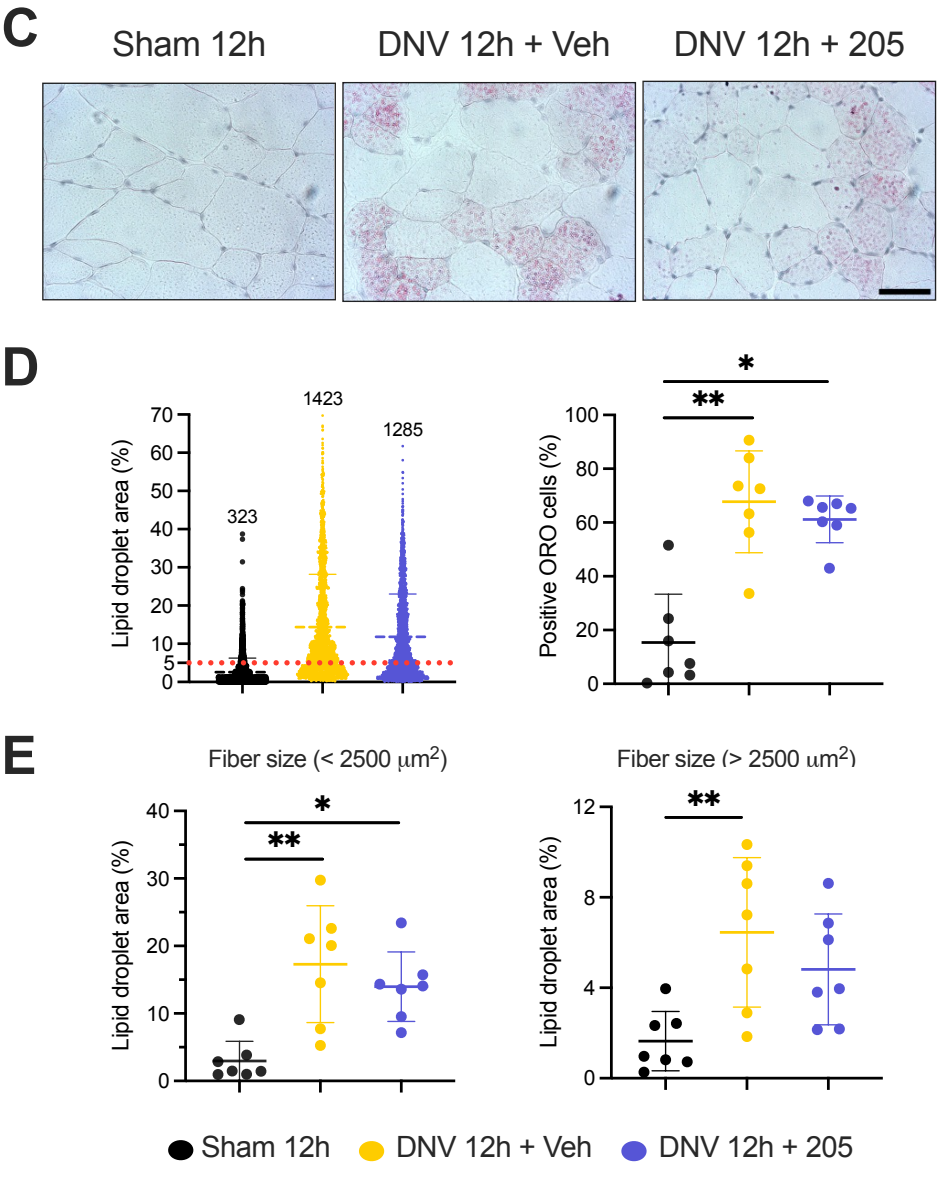
C
Sham 12h
DNV 12h + Veh
DNV 12h + 205
D
Lipid droplet area (%)
323
1423
1285
Positive ORO cells (%)
E
Fiber size (< 2500 μm²)
Fiber size (> 2500 um²)
Lipid droplet area (%)
Sham 12h
DNV 12h + Veh
DNV 12h + 205

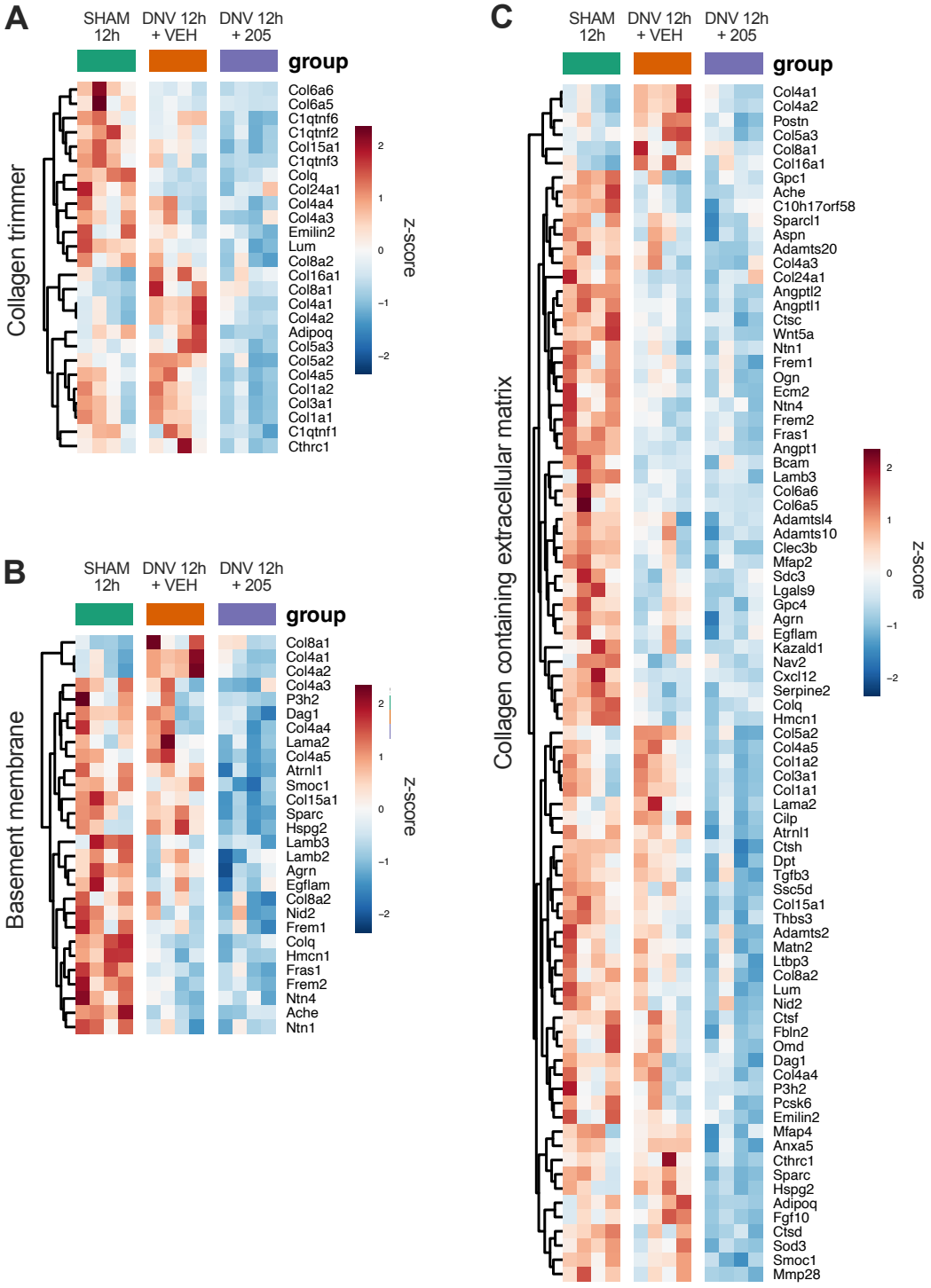
A
SHAM 12h
DNV 12h + VEH
DNV 12h + 205
group
Collagen trimmer
Col6a6
Col6a5
C1qtnf6
C1qtnf2
Col15a1
C1qtnf3
Colq
Col24a1
Col4a4
Col4a3
Emilin2
Lum
Col8a2
Col16a1
Col8a1
Col4a1
Col4a2
Adipoq
Col5a3
Col5a2
Col4a5
Col1a2
Col3a1
Col1a1
C1qtnf1
Cthrc1
z-score
2
1
0
−1
−2
B
SHAM 12h
DNV 12h + VEH
DNV 12h + 205
group
Basement membrane
Col8a1
Col4a1
Col4a2
Col4a3
P3h2
Dag1
Col4a4
Lama2
Col4a5
Atrnl1
Smoc1
Col15a1
Sparc
Hspg2
Lamb3
Lamb2
Agrn
Egflam
Col8a2
Nid2
Frem1
Colq
Hmcn1
Fras1
Frem2
Ntn4
Ache
Ntn1
z-score
2
1
0
−1
−2
C
SHAM 12h
DNV 12h + VEH
DNV 12h + 205
group
Collagen containing extracellular matrix
Col4a1
Col4a2
Postn
Col5a3
Col8a1
Col16a1
Gpc1
Ache
C10h17orf58
Sparcl1
Aspn
Adamts20
Col4a3
Col24a1
Angptl2
Angptl1
Ctsc
Wnt5a
Ntn1
Frem1
Ogn
Ecm2
Ntn4
Frem2
Fras1
Angpt1
Bcam
Lamb3
Col6a6
Col6a5
Adamtsl4
Adamts10
Clec3b
Mfap2
Sdc3
Lgals9
Gpc4
Agrn
Egflam
Kazald1
Nav2
Cxcl12
Serpine2
Colq
Hmcn1
Col5a2
Col4a5
Col1a2
Col3a1
Col1a1
Lama2
Cilp
Atrnl1
Ctsh
Dpt
Tgfb3
Ssc5d
Col15a1
Thbs3
Adamts2
Matn2
Ltbp3
Col8a2
Lum
Nid2
Ctsf
Fbln2
Omd
Dag1
Col4a4
P3h2
Pcsk6
Emilin2
Mfap4
Anxa5
Cthrc1
Sparc
Hspg2
Adipoq
Fgf10
Ctsd
Sod3
Smoc1
Mmp28
z-score
2
1
0
−1
−2